# Looking Inside Poly(*N*-isopropylacrylamide) Microgels: Nanomechanics and Dynamics at Solid-Liquid Interfaces

Judith Witte,[†] Tetyana Kyrey,[‡] Jana Lutzki,[†] Anna Margarethe Dahl,[†] Matthias Kühnhammer,[¶] Regine von Klitzing,[¶] Olaf Holderer,[‡] and Stefan Wellert[*,†]

[†]*Technische Universität Berlin, Department of Chemistry, 10623 Berlin, Germany*

[‡]*Forschungszentrum Jülich GmbH, Jülich Centre for Neutron Science at MLZ, 85748 Garching, Germany*

[¶]*Technische Universität Darmstadt, Department of Physics, 64289 Darmstadt, Germany*

E-mail: s.wellert@tu-berlin.de

**Abstract**

The continuous improvement of synthesis leads to a great variety in the internal architecture and functionality of colloidal hydrogels. A majority of envisioned applications uses microgels as colloidal building blocks for the layer formation at solid substrates. In this context, a fundamental understanding of the influence of these substrates on the internal structure and physical properties is essential. Especially, nanomechanical properties of adsorbed poly(*N*-isopropylacrylamide) microgel particles are important for their application in cell cultivation, functional surface coatings and others. Furthermore, these properties are closely related to the swelling behavior and the internal structure and dynamics of these microgels. However, the number of methods that are able to probe the viscoelasticity of adsorbed microgels over the entire vertical particle

profile is limited. Grazing incidence neutron scattering techniques are suited to probe soft matter samples with limited sample volumes at planar solid substrates, and allow a resolution in $z$-direction. We used neutron spin echo spectroscopy under grazing incidence to access fast thermal fluctuations ($10^{-9}$ s) over the entire vertical particle profile. Atomic force microscopy nanoindentation was used to characterize the nanomechanical properties of adsorbed microgel particles prepared by a batch and a continuous monomer feeding method. Resulting force maps revealed that batch-microgels were "hard" and heterogeneous in their Young's moduli, while microgels from the continuous method were "soft" and homogeneous. Finally, neutron spin echo spectroscopy under grazing incidence revealed major differences in the vertical dynamic profile of both types of microgels.

# Introduction

Poly($N$-isopropylacrylamide) (PNIPAM) microgels are thermoresponsive materials that combine the properties of colloids (size, colloidal stability) and porous hydrogels (swollen by solvent, soft and deformable).[1] Due to this nature, they are widely discussed for applications in bulk and as coating materials.[2,3] It has been shown that the internal dynamics and viscoelastic properties are important for the diffusion of guest molecules and guest particles through a polymer network.[4]

Conventionally, PNIPAM-based microgels are prepared by precipitation polymerization with a batch method.[5] However, the batch method yields particles with an inhomogeneous distribution of cross-linking, where a denser core is surrounded by dangling polymer chains. Feeding methods have been developed to influence the polymerization kinetics toward a more homogeneous distribution of cross-links.[6–8]

A variety of experimental methods ranging from light, X-ray and neutron scattering to atomic force microscopy (AFM) and super-resolution fluorescence microscopy was applied to characterize the structure of microgels usually dispersed in water or confined at solid or

liquid interfaces.[9–13]

Recently, several experimental techniques have been developed to determine the mechanical properties of microgels.[14] For example, in bulk samples, oscillatory shear measurements and osmotic deswelling were applied.[15,16] From the knowledge of their mechanical properties conclusions can be drawn on their interparticle interactions in a wide volume fraction range.[17] Confinement to a solid substrate enables the use of AFM techniques to explore changes compared to the bulk and the characterization of individual microgel particles is possible. The stiffness of a microgel particle is influenced by the molar ratio of monomer to cross-linker during the polymerization. A higher degree of cross-linking leads to stiffer particles. Moreover, the cross-linker distribution influences the stiffness of adsorbed microgel particles. Matsui *et al.* showed in high-speed AFM studies that softer microgel particles, due to their higher deformability, adsorb faster than harder elastomeric or rigid microspheres on solid substrates.[18] This has important implications for biomedical applications where microgel spheres should adsorb on diseased sites, such as carcinoma. Mihut *et al.* showed that soft colloidal particles adsorbed well on lipid membranes.[19]

Furthermore, the viscoelasticity of the microgel particles affects cell adhesion. Saxena *et al.* found that the morphology of fibroblasts was majorly impacted by the viscoelastic properties of the microgel layers they were cultured on.[20]

AFM nanoindentation revealed the influence of the dense core on the Young's modulus of adsorbed PNIPAM microgels.[21,22] Schmidt *et al.* observed a nanoscopic gradient of mechanical properties with a maximum Young's modulus in the particles' center. Witt *et al.* found that adsorbed feeding PNIPAM-*co*-AA microgels do not display a gradient in nanomechanical properties and have a constant Young's modulus over the entire particle.[23]

While AFM nanoindentation and fast force mapping are useful techniques to investigate the lateral gradient of nanomechanical microgel properties, they can only probe up to 30% of maximum indentation. This avoids an influence of the hard substrate on the results. Therefore, a comprehensive look into the network that reveals the mechanics over the en-

tire vertical particle profile is lacking. As described for example by the Tanaka-Filmore approach for the inner dynamics of spherical gels the density fluctuations inside the polymer network are directly related to the mechanical constants of the polymer network.[24] Hence, measurements of the polymer dynamics inside microgels can reveal additional information. As reported in literature, neutron spin echo spectroscopy (NSE) is a suitable scattering technique to explore the dynamics in microgel dispersions and inside adsorbed microgel particles.[25–27] We employed neutron spin echo spectroscopy under grazing incidence (GINSES) to probe the internal dynamics of adsorbed PNIPAM-based with comparatively high amounts of cross-linker (10mol%). Microgel particles were prepared with a conventional batch method ("batch-microgels") and a continuous monomer feeding method ("feeding-microgels"). We were curious whether a high amount of cross-linker would stabilize the microgel network in the vicinity of a solid substrate and give it structural integrity. First, we imaged the adsorbed microgel particles in air and in water to gain information about their swelling behavior. Afterwards, fast force maps were recorded to compare the Young's modulus distribution in batch and feeding-microgels. As mentioned above, this provides limited information on the nanomechanical microgel properties perpendicular to the substrate-particle interface. GINSES was used to probe the internal dynamics of near-surface layers and over the entire vertical particle profile. Figure 1 qualitatively illustrates the differences in both methods and the complementary information that can be accessed in such an approach. The obtained data are compared to previously published bulk NSE data,[28] to estimate the influence of the solid surface on the internal microgel dynamics.

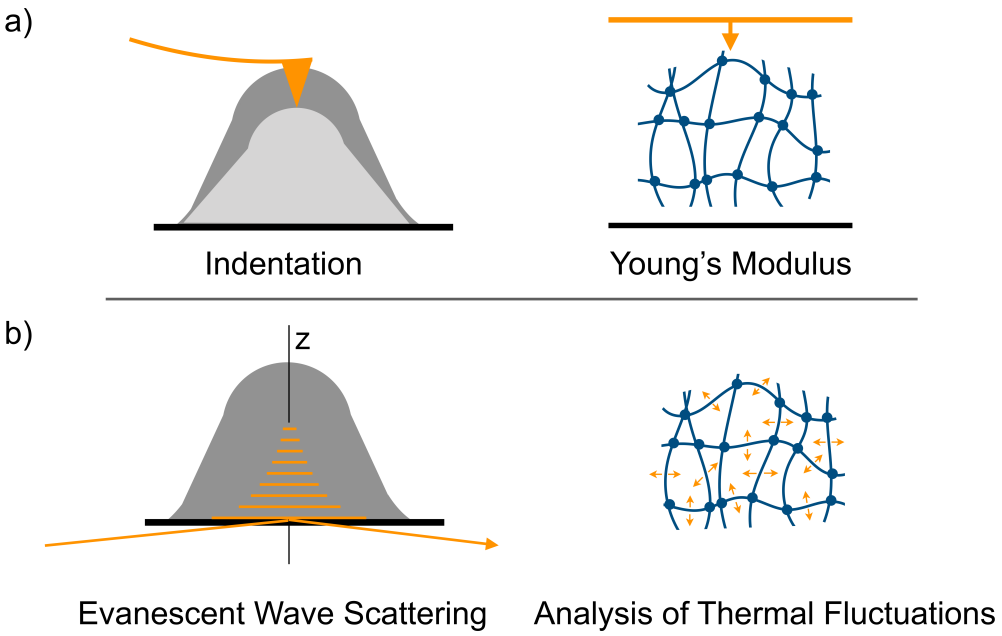


Figure 1: Schematic comparison of the applied experimental techniques. Dark grey indicates the region accessible with the method. a) AFM nanoindentation probes the outer region of a sample in an uniaxial compression which yields the Young's modulus. b) Neutron spin echo under grazing incidence probes the near-surface region by evanescent wave scattering and explores the thermal fluctuations. They can be related to the mechanical constants of the investigated sample.

# Methods

## Materials

*N*-isopropylacrylamide (NIPAM, $\geq$ 99 %), *N,N'*-methylenebisacrylamide (BIS, 99 %) and 2,2'-azobis(2-methylpropionaminidine) dihydrochloride (AAPH, 97 %) were purchased from Sigma-Aldrich. Ethanol abs. was purchased from CHEMSOLUTE®. $D_2O$ was purchased from Deutero. All chemicals were used as received. Water was purified with a MilliQ system (Millipore) with a resistance of 18 MΩ. Silicon wafers were purchased from MicroChemicals. Silicon blocks were purchased from Siliciumbearbeitung Andrea Holm GmbH.

## Preparation of PNIPAM Microgels

Batch and feeding-microgels were prepared by surfactant-free precipitation polymerization as described in our previous publication.[28] Microgels with 10mol% of BIS were studied.

**Batch Method** In a double walled glass reactor, NIPAM (1.527 g, 13.5 mmol) and BIS (0.232 g, 1.5 mmol) were dissolved in 120 mL water. The solution was purged with nitrogen for 60 min at 80 °C under continuous stirring. Afterwards, the positively charged initiator AAPH (68.7 mg, 0.25 mmol) was pre-dissolved in 1 mL water and was added to the solution. The polymerization was quenched after 10 min by release of the solution into an ice-cooled beaker.

**Feeding Method** In order to obtain microgels with a more even cross-link distribution, the method described above was modified according to Acciaro *et al.*[8] The double walled glass reactor was filled with 97.76 mL water. The water was purged with nitrogen for 60 min at 80 °C under continuous stirring. Simultaneously, NIPAM (1.527 g, 13.5 mmol) and BIS (0.232 g, 1.5 mmol) were dissolved in 22.24 mL water and degassed for 60 min as well. Afterwards, pre-dissolved AAPH (68.7 mg, 0.25 mmol) was added to the reactor. Promptly,

a syringe filled with the NIPAM/BIS solution was mounted onto an automated pump. The speed of the monomer feed was 2 mL· $min^{-1}$. The reaction was quenched after 11 min 20 s by release of the solution into an ice-cooled beaker.

**Purification** Regardless of the polymerization method, microgel dispersions were dialysed in a dialysis membrane (MWCO = 14 kDa) for 3 weeks. To remove water the microgel dispersions were lyophilized at -85 °C and 1 mbar.
The sample nomenclature is $MG_xP$ and $MG_xF$, where x is the amount of cross-linker added during the polymerization in mol%. P and F stand for batch and feeding method, respectively.

## Spin-Coating Procedures

Microgel monolayers with a surface coverage of 50-60% were prepared on silicon blocks (50 mm x 80 mm x 15 mm) *via* spin-coating of aqueous dispersions ($c_{MG}$ = 0.25 wt%) at 1000 rpm for 100 s. After spin-coating, the microgel coatings were cured in water over night. AFM force mapping required individual particles on the surface. Consequently, silicon wafers (20 mm x 20 mm) were spin-coated with dilute microgel dispersions ($c_{MG}$ = 0.02 wt%) at 1000 rpm for 100 seconds. (Corresponding AFM topography images are shown in Figures S3 and S7)

## Atomic Force Microscopy

AFM measurements were carried out with a Cypher AFM (Oxford Instruments). AFM images in water and fast force maps were scanned with BL-AC40TS cantilevers (Oxford Instruments) with a spring constant of $k$ = 0.09 N/m and a resonance frequency of $f_{res}$ = 110 $kHz$. Samples were placed in a liquid probe holder and the temperature was set to 20 °C. Force curves were fitted with the Hertz model

$$F = \frac{4E\sqrt{R}}{3(1-\nu^2)} \cdot \delta^{3/2}, \tag{1}$$

where $F$ is the force exerted by a spherical indenter with the radius $R$, $E$ the Young's modulus, $\nu$ the Poisson ratio and $\delta$ the indentation depth. We assumed a Poisson ratio $\nu$ of 0.5. The tip radius was 8 nm. The fit area was 0 - 30% of maximum indentation.

## Modeling of the Evanescent Intensity Distribution and the Penetration Depth

In grazing incidence measurements the intensity $I_{ev}$ is a function of the distance $z$ from the scattering plane and the angle of incidence $\alpha_i$ and $\mathrm{I}_{ev}$=$\mathrm{I}_{ev}$(z,$\alpha_i$). The estimation of $I_{ev}(z, \alpha_i)$ and of the penetration depth $z_{1/e}$ of the evanescent field was done by simulations with BornAgain which uses the framework of the distorted wave Born approximation.[29] In these simulations, $I_{ev}(z, \alpha_i)$ was calculated at a constant neutron wavelength considering the wavelength resolution, layer roughness, and absorption effects of the real experiment. The differences between batch and feeding-microgels were accounted for *via* the implementation of the different bulk correlation length into the model. The impinging neutron beam enters the interface through the silicon block. Simulations of $I_{ev}$ with and without microgels adsorbed at the solid-liquid interface enable to estimate the ratio between sample signal and experimental background. (for details refer to Figures S9, S11 and S12.)

## Grazing Incidence Neutron Spin Echo Spectroscopy

NSE measures the normalized intermediate scattering function $S(Q, \tau_{NSE})/S(Q, 0)$ which is the time Fourier transform of the van Hove pair correlation function. Hence, in soft matter samples NSE probes thermally induced density fluctuations.

Figure 2 illustrates the typical experimental setup of the reflection mode used in a grazing incidence measurement. The neutron beam enters the sample from the silicon side and is

reflected at the silicon-microgel interface. Below the critical angle the evanescent intensity exponentially decays into the sample and measurements become surface-sensitive. Details of the NSE principle are given in the supporting information (refer to Figure S1). The analysis of the final polarization state of the neutrons at the detector yields information about the energy exchange between neutron and sample in the scattering event. These data can be transferred into the intermediate scattering function which can be further evaluated to analyze the dynamics inside the sample. The Fourier time $\tau_{NSE}$ is an instrumental parameter with the dimension of time which can be tuned by changing the strength of the magnetic guiding field.

Combined with grazing incidence scattering geometry, NSE can probe thermal fluctuations along the $z$-direction of adsorbed soft matter samples. GINSES was conducted at the J-NSE "Phoenix" instrument, operated by Forschungszentrum Jülich GmbH, JCNS at MLZ (Garching, Germany).[30] Microgel-coated silicon blocks were immersed in $D_2O$, which provides good contrast between polymer and solvent. The temperature was controlled with a thermostat and was set to 20 °C.

Each sample was measured at two angles of incidence (below and above the critical angle of approximately $\alpha_c = 0.3°$). The neutron wavelength was 6 Å with a distribution of 20%. The experiments covered Fourier times $\tau_{NSE}$ between 0.5 and 35 ns. The scattering vector $Q_{GINSES}$ has a small component in lateral direction which can be neglected here. At the chosen scattering angle mainly the z-component of $Q_{GINSES}$ contributes to the detected signal.

The raw NSE data was treated with the analysis software DrSpine.[31]

The ISFs $S(Q, \tau_{NSE})$ were fitted with a single exponential decay with a relaxation rate $\Gamma_{coop}$

$$S(Q, \tau_{NSE}) = (A_0 - A_{bgr}) \times e^{(-\Gamma_{coop}\tau)} + A_{bgr} \tag{2}$$

to account for the cooperative diffusion of the polymer chains in the microgel's network. The

amplitude value $A_0$ was initially determined and kept fixed during the fitting. We assume that the background level $A_{bgr}$ is the sum of the experimental background $A_{bgr}^{ex}$ considering instrumental contributions to the background and a signal base level $A_{bgr}^{el}$ caused by the elastic scattering of frozen heterogeneities or resulting from rather slow dynamics.

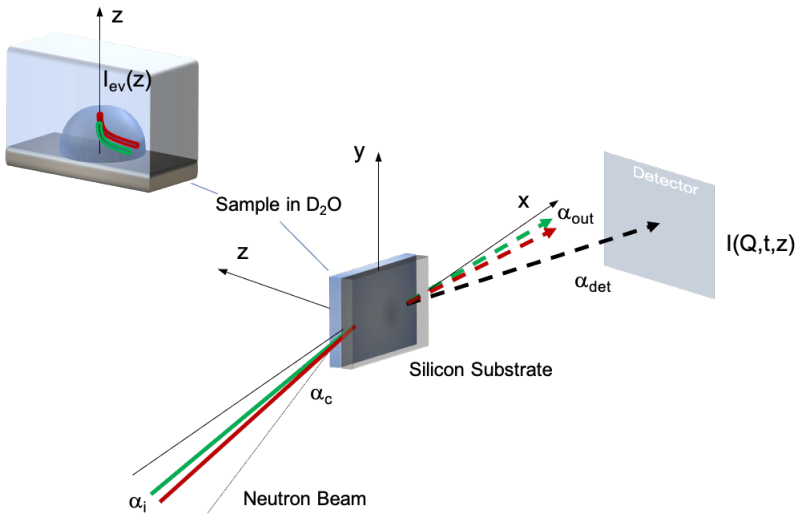


Figure 2: Setup of a GINSES experiment. A neutron beam impinges under a very shallow angle $\alpha_i$ below the critical angle of total external reflection $\alpha_c$ onto the silicon-$D_2O$+microgel interface. Under this condition an evanescent intensity distribution $I_{ev}(z)$ occurs and exponentially decays into the sample volume in z direction perpendicular to the confining surface. At the experimentally accessible values of $Q_{GINSES}$ scattered neutrons from this region are detected at an detection angle $\alpha_{det}>\alpha_c$. Increasing $\alpha_i$ results in larger penetration depths into the sample.

In a transmission mode measurement the intermediate scattering function $S(Q, \tau_{NSE})$ is normalized by measuring $S(Q, 0)$ with a reference sample without any energy exchange with the impinging neutron beam. This standard data treatment fails for grazing incidence measurements in reflection mode. It is hardly possible to find a purely elastically scattering reference sample with the same scattering length density profile as the investigated sample. Therefore, the same experimental conditions as for the sample cannot be set for the reference sample. Hence, the amplitudes $A_0$ of the intermediate scattering function have values $A_0 < 1$. This can also be seen in the GINSES measurement at the $D_2O$-silicon substrate where no decay of the ISF is observable due to mainly elastic scattering (Figure S13).

To estimate the penetration depth $z_{1/e}$ of the evanescent field into the adsorbed microgel layer is given by

$$z_{1/e} = \frac{2^{1/2}\lambda}{4\pi(((\alpha_i^2 - \alpha_c^2)^2 + (\frac{\lambda\mu}{2\pi})^2)^{1/2} - (\alpha_i^2 - \alpha_c^2))^{1/2}}, \quad (3)$$

where $\lambda$ is the neutron wavelength, $\alpha_i$ the angle of incidence, $\alpha_c$ the critical angle of total external reflection and $\mu$ the absorption coefficient (details for $\mu$ are given in the SI) The critical angle can be determined from neutron reflectometry (for further information refer to Figure S9). Here, $\alpha_c$ can be taken from the position of the critical edge of total reflection. No additional assumptions about the sample composition are required.

# Results and Discussion

In the following, the influence of the internal structure of highly cross-linked microgel particles (10 mol% BIS prepared with a positively charged initiator) on their nanomechanics in the adsorbed state is investigated using a combination of AFM imaging, AFM force mapping and GINSES. While AFM nanoindentation probes the nanomechanical properties of the top region (approximately 30% of maximum indentation) of an individual particle, GINSES has access to the near-surface layers and offers $z$-resolution (Figure 1). We chose PNIPAM-based microgel particles with different internal structures prepared with (i) a conventional batch method and (ii) a continuous feeding method as represantitives for "hard" and "soft" microgels.

## Swelling Behavior of Adsorbed Batch and feeding-microgels

The aspect ratios (width:height) of batch ($MG_{10}P$) and feeding ($MG_{10}F$) microgels in the adsorbed state and the particles' swelling capability can be extracted from AFM topographies (Figures 3 and 4). We observe a severe collapse of $MG_{10}F$ in the adsorbed dry state expressed by an aspect ratio of 25. In comparison, $MG_{10}P$ has an aspect ratio of 4 in the dry state. In the swollen state the aspect ratios reduce to 2.4 and 5 for $MG_{10}P$ and $MG_{10}F$, respectively.

The high change in aspect ratio for the feeding-microgel shows that despite the severe collapse in the dry state, swelling of the polymer network is still observed. We conclude that the absence of a highly cross-linked core region leads to a densification and compression of the feeding-microgel in the dry adsorbed state. However, in the batch-microgel particles the highly cross-linked core region acts as a scaffold, giving them more structural integrity after adsorption. Height cross-sections of $MG_{10}F$ and $MG_{10}P$ are displayed in Figures 3 and 4.

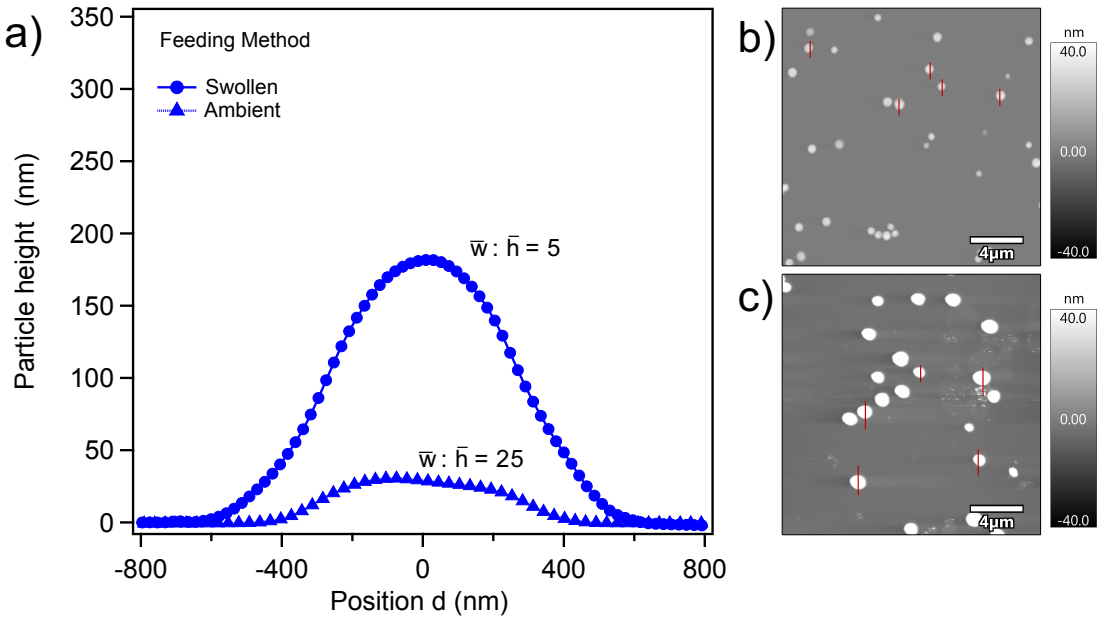


Figure 3: a) Cross-sections from AFM topography images (20 x 20 $\mu m^2$) of the adsorbed feeding-microgel $MG_{10}F$ in the ambient state (b) and swollen in water at 20 °C (c). Cross-sections were calculated from the average of 5 individual particles.

A comparison of the volumes calculated from dynamic light scattering (DLS) in bulk and from AFM images further supports these findings. The volume $V_{DLS}$ of a sphere with hydrodynamic radius $R_h$ is compared to the volume $V_{AFM} = (\pi h_{AFM}/6)(3(w_{AFM}/2)^2 + h_{AFM}^2)$ of a segmented ball with the measured height $h_{AFM}$ and width $w_{AFM}$ of the adsorbed microgels. The volume of a sphere of $MG_{10}F$ is 8 times larger in bulk than in the adsorbed state. For $MG_{10}P$ the bulk volume is only 1.4 times larger than the volume in the adsorbed swollen state. Table 1 lists the results of DLS and AFM measurements.

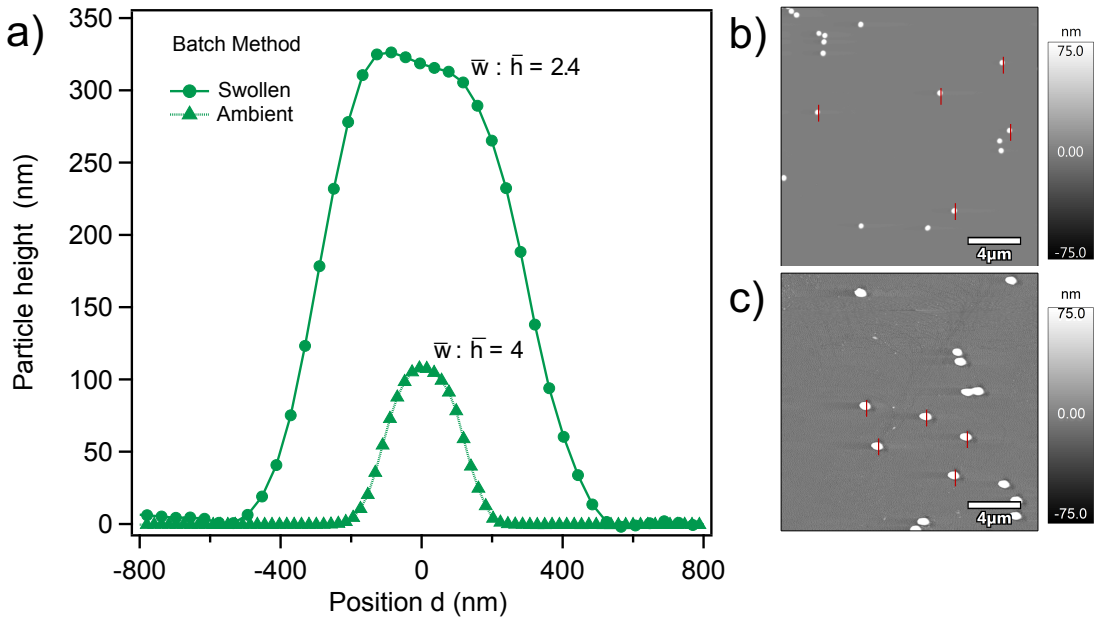


Figure 4: a) Cross-sections from AFM topography images (20 x 20 $\mu m^2$) of the adsorbed batch-microgel $MG_{10}P$ in the ambient state (b) and swollen in water at 20 °C (c). Cross-sections were calculated from the average of 5 individual particles.

## Nanomechanics from AFM Fast Force Mapping

Force maps and the extracted cross-sections (Figure 5) illustrate the different distribution of the Young's modulus $E$ in both types of microgels. The batch-microgel has a maximum Young's modulus in the center ($d = 0$), which decreases to 1/3 of the maximum value towards the edge of the particle. This supports the hypothesis that the particle core acts as a stabilizing scaffold in the adsorbed state. In comparison, the feeding-microgel displays no such stiffness gradient. Instead, Young's moduli vary between approximately 50 and 100 kPa without a maximum in the center. We conclude that the feeding-microgel lacks a dense core, and is much softer overall.

Knowledge of at least two material constants enables the calculation of all other related material constants. For example, the Young's modulus can be derived from the bulk modulus $K$ and Poisson's ratio $\nu$ according to $E = 3K(1 - 2\nu)$. Assuming Poisson ratios for both microgels in the range $0.25 < \nu < 0.4$ as reported in the literature,[32–34] large bulk moduli between 400 kPa and 1 MPa for $MG_{10}P$ and between 70 kPa and 170 kPa for $MG_{10}F$ could

be expected. Consequently, significant differences in the microgel interactions at high volume fractions are very likely as well.

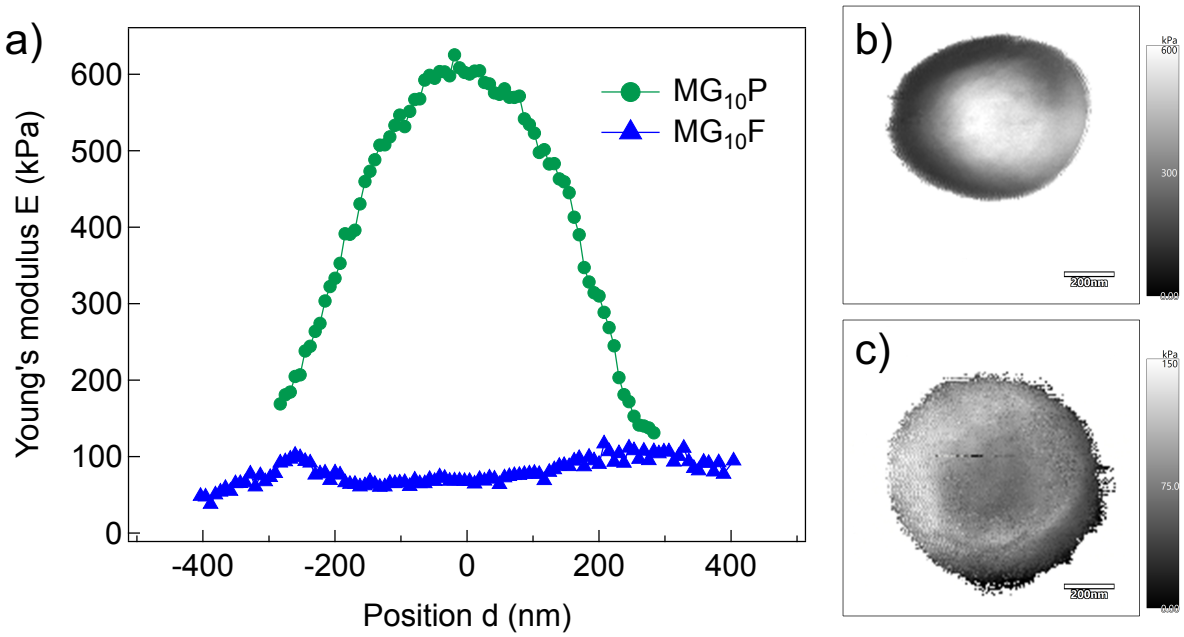


Figure 5: a) Cross-sections of the Young's modulus of $MG_{10}P$ and $MG_{10}F$ in water at 20 °C. Fast force maps of individual PNIPAM microgel particles recorded with the AFM for b) batch and c) feeding microgels.

Table 1: Microgel geometry as determined from DLS and AFM experiments in water at 20 °C. The hydrodynamic volume is $V_{DLS} = 4/3\pi R_h^3$ and the volume of the swollen adsorbed microgel $V_{AFM} = (\pi h_{AFM}/6)(3(w_{AFM}/2)^2 + h_{AFM}^2)$ was approximated as the volume of a segmented ball.

| Sample | $R_h$ (nm) | $V_{DLS}$ $(10^7 nm^3)$ | $w_{AFM}$ (nm) | $h_{AFM}$ (nm) | $V_{AFM}$ $(10^7 nm^3)$ |
|---|---|---|---|---|---|
| $MG_{10}F$ | 463 | 42 | 890 | 178 | 5.8 |
| $MG_{10}P$ | 310 | 13 | 765 | 323 | 9.2 |

## Internal Dynamics of Batch and feeding-microgels

A GINSES experiment probes a system's dynamics perpendicular to a confining substrate (Figure 2).[35] In case of adsorbed microgel particles, the translational center-of-mass diffusion is suppressed, but the swollen network has internal dynamics due to thermal fluctuations. A high ratio of coherent to incoherent scattering intensity is crucial in a GINSES measurement

to keep the background signal at a minimum. Therefore, the ideal momentum transfer with a good signal to background ratio, $Q_{GINSES}$, is determined from elastic diffraction scans (Figure S8). In our case $Q_{GINSES} = 0.06$ Å$^{-1}$. At this rather low $Q$-value the dynamics will be dominated by density fluctuations, whereas segmental polymer chain dynamics would require measurements at shorter length scales (*i.e.* larger $Q_{GINSES}$).

The penetration depth of the evanescent field $z_{1/e}$ at a constant neutron wavelength for a certain sample can be varied with the angle of incidence $\alpha_i$. A gradual increase of $z_{1/e}$ below the critical angle of total external reflection $\alpha_c$ is followed by a steep increase around $\alpha_c$ with increasing angle of incidence.[36] Above $\alpha_c$ the penetration depth virtually reaches infinity compared to typical vertical sample dimensions of 300-400 nm. This is shown in Figure 6A where the calculated values of $z_{1/e}$ are plotted against $\alpha_i$ for $MG_{10}F$. Measurements around $\alpha_c$ are less precise, because of the wavelength distribution $\Delta\lambda/\lambda$, which has a stronger influence on $z_{1/e}$ around $\alpha_c$.[37]

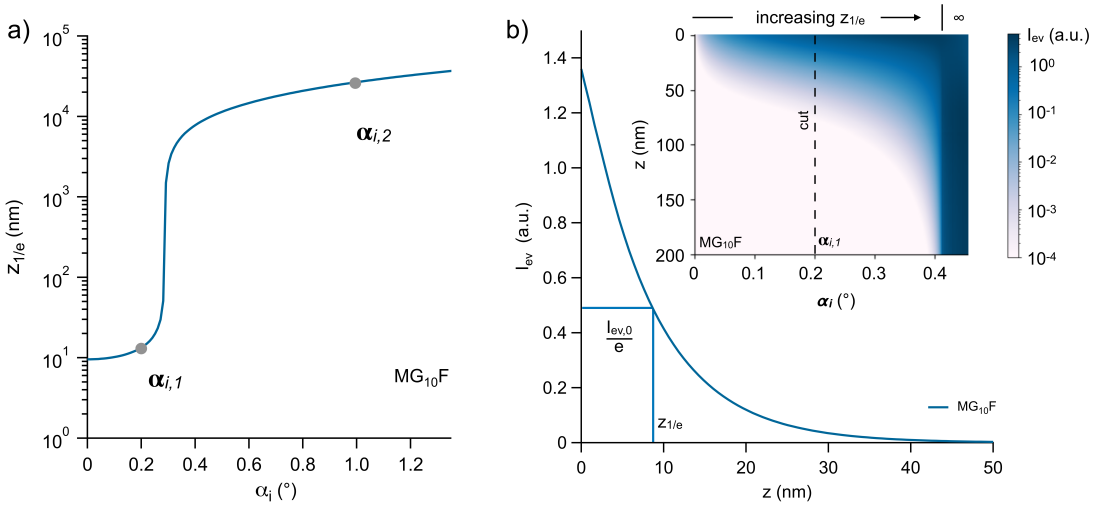


Figure 6: Calculation of the penetration depth $z_{1/e}$ according to equation 3 is shown in plot a) for the example of sample $MG_{10}F$. Results of the simulations with BornAgain are summarized in b) for sample $MG_{10}F$. The inset shows the distribution of the evanescent intensity as a function of the vertical distance $z$ from the substrate and the angle of incidence $\alpha_i$. From cuts at a constant value of $\alpha_i$ the decay of $I_{ev}(z)$ and the penetration depth $z_{1/e}$ can be extracted.

Recently, simulations with BornAgain were used to calculate the evanescent intensity distribution $I_{ev}(z, \alpha_i)$. This is exemplified in Figure 6B where $I_{ev}(z, \alpha_i)$ is shown for $MG_{10}F$. By cutting this distribution along $z$ at constant $\alpha_i$ the decay of the evanescent intensity was extracted. (Results for $MG_{10}P$ are given in Figure S11.) Those simulations help to determine the penetration depth of the evanescent field ($I_{ev}$ drops to $I_{ev}/e$) and provide information about the experimental background, otherwise hardly accessible in a grazing incidence setup.[29] The simulations take into account the experimental conditions such as the wavelength distribution, scattering geometry and the particular scattering properties of the sample. (Results from simulations of the background in the small angle scattering under grazing incidence are shown in Figure S12.)

Intermediate scattering functions (ISF) $S(Q, \tau_{NSE})$, with $\tau_{NSE}$ the Fourier time, below ($z_{1/e}$=10 nm) and above ($z_{1/e} \rightarrow \infty$) the critical angle $\alpha_c$ demonstrate differences between $MG_{10}F$ and $MG_{10}P$ (Figures 7 and 8). $MG_{10}F$ has a rather flat ISF at a low penetration depth and hence in vicinity to the surface. As the penetration depth increases to virtually infinity, the ISF declines over $\tau_{NSE}$. In contrast, the ISFs of $MG_{10}P$ show a decline of $S(Q, \tau_{NSE})$ with $\tau_{NSE}$ for both penetration depths (Figure 8). This observation can be quantified by fitting the data according to equation 2 and the following deliberation.

The experimental background present in the ISFs contains additional information about the inner structure and dynamics of the adsorbed microgels. We assume that the background $A_{bgr}$ consists of the experimental background $A_{bgr}^{ex}$ and a signal base level $A_{bgr}^{el}$ as described in the methods section. Simulations (see also Figure S12) show that the contribution of the silicon/$D_2O$ interface is negligible. This justifies the assumption $A_{bgr} \approx A_{bgr}^{el}$. If we further assume that the overall amplitude $A_0$ is the sum of a contribution from density fluctuations in the sample $A_s$ and the background $A_{bgr} \approx A_{bgr}^{el}$, we can calculate and compare the contribution of $A_s$ and $A_{bgr}$ to $A_0$.

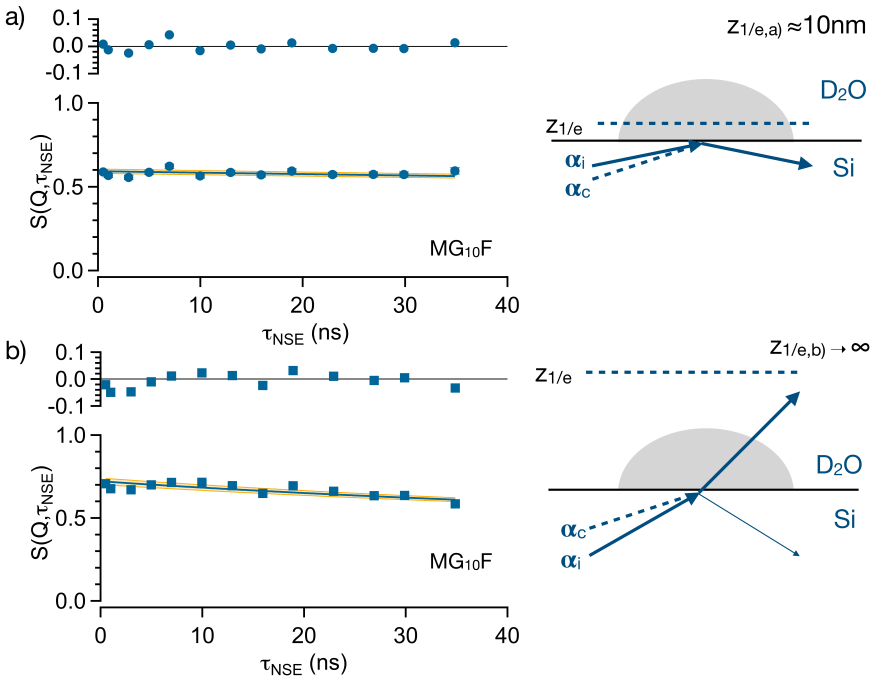


Figure 7: ISFs of $MG_{10}F$ measured in reflection geometry at $Q_{GINSES}$=0.06 Å$^{-1}$ at a penetration depth $z_{1/e}$ of a) $z_{1/e,a} = 10\ nm$ and b) $z_{1/e,b} \to \infty$. The solid lines are fits of equation 2 to the measured data. Additionally, the confidence interval of the fit and the residuals are shown for both graphs.

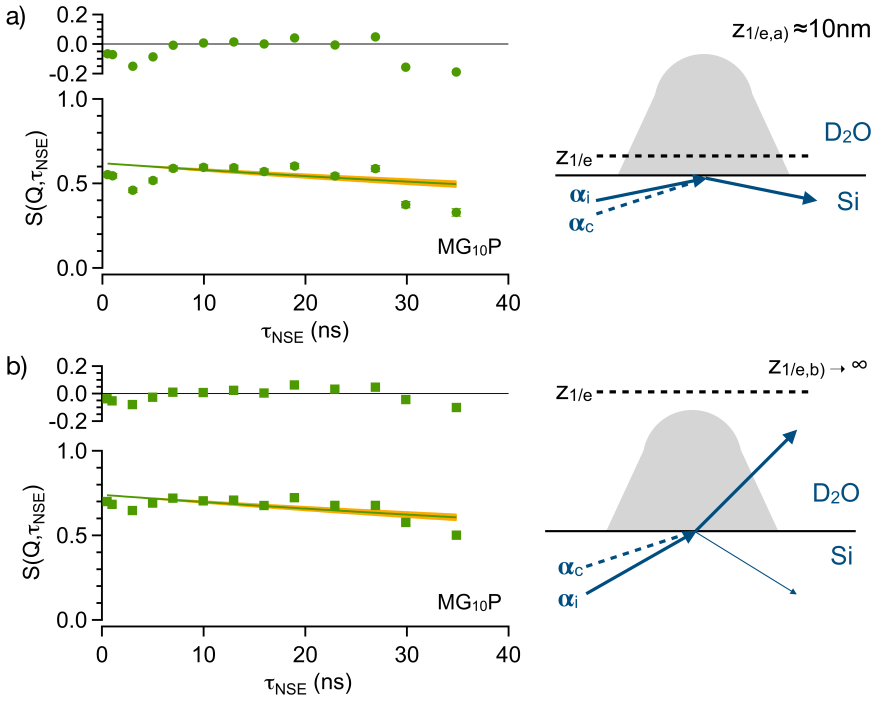


Figure 8: ISFs of $MG_{10}P$ measured in reflection geometry at $Q_{GINSES}$=0.06Å$^{-1}$ at a penetration depth $z_{1/e}$ of a) $z_{1/e,a}$=10 nm and b) $z_{1/e,b} \rightarrow \infty$. The solid lines are fits of equation 2 to the measured data. Additionally, the confidence interval of the fit and the residuals are shown for both graphs.

Details of the fits to the GINSES data of adsorbed $MG_{10}F$ and $MG_{10}P$ microgel particles according to equation 2 are summarized in Table S1 in the supporting information. In the near-surface layers of the feeding-microgel, $A_{bgr} \approx A_{bgr}^{el}$ and $A_s$ both contribute 50% to $A_0$. However, the contribution from elastic scattering increases to 62% when the entire vertical profile is probed. At the same time, the contribution from density fluctuations decreases to 38%. In near-surface layers of $MG_{10}P$ density fluctuations and elastic scattering contribute 68% and 32%, respectively . At virtually infinite penetration depth, those values remain roughly the same with 66% and 34%. In conclusion, the feeding-microgel has a higher contribution of elastic scattering where thermal energy does not suffice to excite density fluctuations of the polymer network in vicinity to the surface.

The cooperative diffusion coefficient $D_{coop}$ is calculated from the relaxation rate $\Gamma_{coop} = D_{coop}Q^2_{GINSES}$ and describes the thermal network density fluctuations. We find a value of $D_{coop}$ = (0.8±0.2)x$10^{-7}$ cm$^2$/s for the feeding-microgel within the first 10 nm from the solid surface. This is a dramatic decrease compared to the bulk value of (4.98±0.04)x$10^{-7}$ cm$^2$/s as we previously published for a microgel in a bulk experiment in transmission geometry [28] (selected ISFs for the low $Q$-range are plotted in Figure S2). Looking at virtually infinite penetration depth we find a much higher value of $D_{coop}$ = (4.2±0.3)x$10^{-7}$ cm$^2$/s which approaches bulk dynamics. $D_{coop}$ of the batch-microgel is identical within the confidence interval for both penetration depths. Moreover, the values are comparable to the bulk value of (2.69±0.02)x$10^{-7}$ cm$^2$/s (Table 2). It appears that the confinement influences the internal dynamics of batch-microgels less compared to softer feeding-microgels.

In the Tanaka-Fillmore description of the swelling kinetics of spherical gels, small displacements in the gel network are analyzed in a linearized elasticity model. [24] The magnitude of these network displacements follows a simple diffusion equation for the diffusive motion of the network in an immobile solvent yielding the cooperative diffusion coefficient

$$D_{coop} = \frac{K + 4/3G}{f}, \tag{4}$$

where $D_{coop}$ is determined by the osmotic bulk modulus $K$, the shear modulus $G$ and the friction coefficient $f$ for the relative motion of the polymer network and the surrounding water. Tanaka and Fillmore limit the validity of their model to an increase of gel radii by a factor of 2 during swelling. They argued, that at larger changes of the gel radii Hook's law is no longer applicable for the description of gel elasticity.

Bearing in mind that the hydrodynamic radius of microgels can increase up to a factor of 2 during swelling, we use the Tanaka-Fillmore approach for a qualitative discussion of the network dynamics in the investigated microgel systems. Based on this description, we attribute the decrease of $D_{coop}$ of $MG_{10}F$ at $z_{1/e}$=10 nm to an increase of the friction coefficient

*f*. Since $f \propto \eta/\xi_{coop}$ is proportional to the solvent viscosity and inversely proportional to the square of the mean correlation length $\xi_{coop}$[38] we interpret the decrease of $D_{coop}$ as an increase of the effective solvent viscosity which is possibly related to increasing polymer segment interactions and an relative decrease of free water inside the network. Based on the results of the NSE measurements with bulk samples of $MG_{10}F$ and $MG_{10}P$,[28] we estimate the relative increase of the effective viscosity in the microgel network $\eta_{eff}/\eta_0$ using the dynamic viscosity $\eta_0 = 1.251$ cP for $D_2O$ at T = 20 °C. These values are listed in Table 2. This change is possibly caused by compression and densification of the polymer network near the solid-liquid interface.

Additional GINSES and AFM measurements of $MG_5P$ (batch-microgel with a cross-linker concentration of 5 mol%) are included in the Supporting Information (Figures S4 to S6, and S10). The lateral distribution of the Young's modulus shows the same features as sample $MG_{10}P$ but with a lower maximum value of approximately 200 kPa. This is in qualitative agreement with a recent AFM nanoindentation study in which the increase of the Young's modulus with increasing cross-linker amount was described with a power law.[21] On the other hand, the internal network dynamics are similar to those of $MG_{10}F$. In near-surface layers a flat ISF indicates suppressed dynamics due to interactions with the solid substrate.

Table 2: Summary of the diffusion coefficients $D_{coop}$=$\Gamma_{coop}/Q^2$ and the relative viscosity $\eta_{eff}/\eta_0$. [a] values were taken from[28]

| sample | measurement | $z_{1/e}$ (nm) | $D_{coop}$ ($10^{-7}$cm$^2$/s) | $\eta_{eff}/\eta_0$ |
|---|---|---|---|---|
| $MG_{10}F$ | bulk | - | 4.98±0.04[a] | 1 [a] |
| | adsorbed | 10 | 0.8±0.2 | 10 |
| | adsorbed | $\infty$ | 4.2±0.3 | 1.2 |
| $MG_{10}P$ | bulk | - | 2.69±0.02[a] | 1 [a] |
| | adsorbed | 10 | 2.8±0.3 | 1.2 |
| | adsorbed | $\infty$ | 2.5±1.3 | 1.2 |

We further observe a minute increase of $S(Q, \tau_{NSE})$ up to 10 ns, which can be attributed to incoherent scattering from hydrogen atoms near the substrate due to the inversion of the

polarization by incoherent scatterers. Therefore, the fitting model was extended by an exponential factor containing the incoherent relaxation rate $\Gamma_i$. The averaged diffusion coefficient hence calculated is $D_i = (1.5\pm0.8)\text{x}10^{-9}$ m$^2$/s. This value likely describes the diffusion of water molecules inside PNIPAM microgels,[39] which might be trapped in near-surface layers. However, this does not influence the results of our previous analysis.

In this paper, we used neutron spin echo spectroscopy under grazing incidence to probe the internal dynamics of adsorbed microgel particles with different internal structures. This method allows to draw conclusions about the internal nanomechanics over the entire particle height. The results indicate that the deformation upon adsorption to a solid surface of soft microgel particles with a homogeneous cross-link distribution leads to a dense polymer layer with suppressed dynamics in close proximity to the surface. At infinite penetration depth the dynamics approach bulk dynamics. In contrast, harder microgel particles with a highly cross-linked core and a fluffy shell display similar dynamics in the bulk and in the adsorbed state, independent of the penetration depth. This suggests a scaffold-like nature of the core region. Therefore, the internal dynamics in vicinity to a solid substrate differ strongly for soft, homogeneous, and harder, inhomogeneous microgel particles.

The high amount of cross-linker does not prevent adsorbed soft, homogeneous microgels from forming a dense polymer layer in vicinity to the surface. This is indicated by the high aspect ratio, extracted from AFM topography, which quantifies the deformation of the microgel particles upon adsorption. Therefore, the higher loading capacity of feeding-microgels in bulk[23] does not necessarily translate to surface applications. This can be disadvantageous for applications in which a load is applied after adsorption of microgels to a surface, because a fraction of the particle volume is not accessible for the guest molecules or particles. However, it could be of advantage in applications where a load is incorporated into a microgel in bulk which then attaches to a surface for controlled release. As was shown by Matsui *et al.* soft, deformable microgels attach faster to solid surfaces than elastomeric or hard spheres.[18]

Previous studies on batch and feeding-microgels also found a distribution of Young's moduli and a constant Young's modulus for batch and feeding-microgels, respectively. In contrast to our results, Witt *et al.* observed that feeding-microgels had a constant Young's modulus that was higher compared to the maximum Young's modulus of batch-microgels. However, the investigated microgels were synthesized with a positively charged comonomer and had a lower cross-linker content.[23] Our GINSES results are in agreement with a study of microgels based on polyethylene glycol with a rather low concentration of cross-linker. The study found an increase in the relaxation rates with increasing distance from the surface, as well.[40] This compares well to our findings for homogeneous, highly cross-linked PNIPAM microgels. In recent years, instrumental improvements at the J-NSE instrument have improved measurement conditions for grazing incidence experiments. This allows to reach higher Fourier times and a realistic time frame for decent statistics at low penetration depths with a smaller scattering volume. However, the $z$-resolution is still limited, as penetration depths around the critical angle cannot be resolved, because the wavelength distribution is critical for sufficient beam intensity. Furthermore, grazing incidence experiments remain time consuming due to low scattering intensities of small scattering volumes. Still, extended acquisition times allowed us to measure the dynamic profiles of adsorbed microgels at two distinct penetration depths and revealed differences between soft and hard microgel particles.

In the future, we expect further instrumental improvements to increase the signal-to-noise ratio and hence, shorten acquisition times. More systematic studies of different systems will become possible. The wavelength distribution at a spallation source can be corrected by a prism, which provides higher beam intensities and an improved control of the angles of incidence.[41] Furthermore, a reduction of incoherent background scattering might enable measurements at different $Q$-values, which allows to expand the observation from cooperative network fluctuations to Zimm-type polymer segment dynamics. Moreover, combining AFM techniques with grazing incidence scattering methods enables the investigation of the influence of solid surfaces on the inner structure and dynamics of even complex polymer

architectures.

## Conclusion

In summary, we used GINSES to elucidate the internal dynamics of adsorbed batch- and feeding-microgels in regions and on time scales inaccessible by other techniques like AFM nanoindentation and/ or evanescent wave DLS (EWDLS). The combination of neutron scattering with the grazing incidence geometry allowed us to distiguish between near-surface layers and the entire vertical particle profile. This method therefore complements AFM nanoindentation which probes only the material's nanomechanical properties, but does not account for the influence of the substrate. Those findings have important implications for the choice of batch or feeding-microgels in applications, especially those where microgels are used as nanocarriers or nanocontainers. While the soft nature of feeding-microgels might be advantageous for certain applications, their deformation at the substrate-particle interface may reduce their effective loading capacity, rendering batch-microgels more suitable in those cases.

## Acknowledgement

The authors thank E. Vezhlev for support with neutron reflectometry measurements and data analysis. Furthermore, we thank M. Ganeva for advice on simulations with BornAgain. We extent thanks to L. Stingaciu, the instrument responsible for the neutron spin echo instrument at the spallation source at Oak Ridge National Laboratory, as well. This work is based upon experiments performed at the J-NSE "Phoenix" operated by JCNS at Heinz Maier-Leibnitz Zentrum (MLZ), Garching, Germany. Funding for this work was granted by Deutsche Forschungsgesellschaft DFG (grant numbers WE5066/3-1 (S. Wellert) and HO5488/2-1 (O. Holderer)).

## Supporting Information Available

The following files are available free of charge.

- WitteSIACSNano2020.pdf: NSE bulk data, neutron reflectivity curves, additional AFM data, additional GINSES data, BornAgain simulation details

## References


(1) Lyon, L. A.; Fernandez-Nieves, A. The Polymer/Colloid Duality of Microgel Suspensions. *Annu. Rev. Phys. Chem.* **2012**, *63*, 25–43.

(2) Plumper, A., Felix; Richtering, W. Functional Microgels and Microgel Systems. *Acc. Chem. Res.* **2017**, *50*, 131–140.

(3) Dai, Z.; Ngai, T. Microgel Particles: The Structure-Property Relationships and their Biomedical Applications. *J. Polym. Sci. A* **2013**, *51*, 2995–3003.

(4) Amsden, B. Solute Diffusion in Hydrogels. An Examination of the Retardation Effect. *Polymer Gels and Networks* **1998**, *6*, 13–43.

(5) Pelton, R. Temperature-Sensitive Aqueous Microgels. *Adv. Colloid Interf. Sci.* **2000**, *85*, 1–33.

(6) Meyer, S.; Richtering, W. Influence of Polymerization Conditions on the Structure of Temperature-Sensitive Poly(*N*-isopropylacrylamide) Microgels. *Macromolecules* **2005**, *38*, 1517–1519.

(7) Wolff, H. J. M.; Kather, M.; Breisig, H.; Richtering, W.; Pich, A.; ; Wessling, M. From Batch to Continuous Precipitation Polymerization of Thermoresponsive Microgels. *ACS Appl. Mater. Interfaces* **2018**, *10*, 24799–24806.

(8) Acciaro, R.; Gilányi, T.; Varga, I. Preparation of Monodisperse Poly(*N*-isopropylacrylamide) Microgel Particles with Homogeneous Cross-Link Density Distribution. *Langmuir* **2011**, *27*, 7917–7925.

(9) Boon, N.; Schurtenberger, P. Swelling of Micro-Hydrogels with a Crosslinker Gradient. *Phys. Chem. Chem. Phys.* **2017**, *19*, 23740–23746.

(10) Karg, M.; Hellweg, T. New "Smart" Poly(NIPAM) Microgels and Nanoparticle Microgel Hybrids: Properties and Advances in Characterisation. *Curr. Opin. Colloid Interface Sci.* **2009**, *14*, 438–450.

(11) Karg, M.; Pich, A.; Hellweg, T.; Hoare, T.; Lyon, L. A.; Crassous, J. J.; Suzuki, D.; Gumerov, R. A.; Schneider, S.; Potemkin, I. I.; Richtering, W. Nanogels and Microgels: From Model Colloids to Applications, Recent Developments, and Future Trends. *Langmuir* **2019**, *20*, 6231–6255.

(12) Wellert, S.; Richter, M.; Hellweg, T.; von Klitzing, R.; Hertle, Y. Responsive Microgels at Surfaces and Interfaces. *Z. Phys. Chem.* **2015**, *229*, 1225–1250.

(13) Scheffold, F. Pathways and Challenges towards a Complete Characterization of Microgels. *Nat. Commun.* **2020**, *11*, 4315.

(14) Backes, S.; von Klitzing, R. Nanomechanics and Nanorheology of Microgels at Interfaces. *Polymers* **2018**, *9*, 1–23.

(15) Conley, G. M.; Zhang, C.; Aebischer, P.; Harden, J. L.; Scheffold, F. Relationship between Rheology andSstructure of Interpenetrating, Deforming and Compressing Microgels. *Nat. Commun.* **2019**, *10*, 1–8.

(16) Sierra-Martin, B.; Frederick, J. A.; Laporte, Y.; Markou, G.; Liter-Santos, J. J.; Fernandez-Nieves, A. Determination of the Bulk Modulus of Microgel Particles. *Colloid Polym. Sci.* **2011**, *289*, 721–728.

(17) de Aguiar, I. B.; van de Laar, T.; Meireles, M.; Bouchoux, A.; Sprakel, J.; Schroën, K. Deswelling and Deformation of Microgels in Concentrated Packings. *Sci. Rep.* **2017**, *7*, 10223.

(18) Matsui, S.; Kureha, T.; Hiroshige, S.; Shibata, M.; Uchihashi, T.; Suzuki, D. Fast Adsorption of Soft Hydrogel Microspheres on Solid Surfaces in Aqueous Solution. *Angew. Chem., Int. Ed.* **2017**, *56*, 12146–12149.

(19) Mihut, A. M.; Dabkowska, A. P.; Crassous, J. J.; Schurtenberger, P.; Nylander, T. Tunable Adsorption of Soft Colloids on Model Biomembranes. *ACSNano* **2013**, *7*, 10752–10763.

(20) Saxena, S.; Hansen, C. E.; Lyon, L. A. Microgel Mechanics in Biomaterial Design. *Acc. Chem. Res.* **2014**, *47*, 2426–2434.

(21) Aufderhorst-Roberts, A.; Baker, D.; Foster, R. J.; Cayre, O.; Mattsson, J.; Connell, S. D. Nanoscale Mechanics of Microgel Particles. *Nanoscale* **2018**, *10*, 16050–16061.

(22) Schmidt, S.; Zeiser, M.; Hellweg, T.; Duschl, C.; Fery, A.; Möhwald, H. Adhesion and Mechanical Properties of PNIPAM Microgel Films and Their Potential Use as Switchable Cell Culture Substrates. *Adv. Funct. Mater.* **2010**, *20*, 3235–3243.

(23) Witt, M. U.; Hinrichs, S.; Möller, N.; Backes, S.; Fischer, B.; von Klitzing, R. Distribution of $CoFe_2O_4$ Nanoparticles Inside PNIPAM-Based Microgels of Different Cross-Linker Distributions. *J. Phys. Chem. B* **2019**, *123*, 2405–2413.

(24) Tanaka, T.; Filmore, D. J. Kinetics of Swelling of Gels. *J. Chem. Phys.* **1979**, *70*, 1214–1218.

(25) Scherzinger, C.; Holderer, O.; Richter, D.; Richtering, W. Polymer Dynamics in Re-

sponsice Microgels: Influence of Cononsolvency and Microgel Architecture. *Phys. Chem. Chem. Phys.* **2012**, *14*, 2762–2768.

(26) Hertle, Y.; Zeiser, M.; Fouquet, P.; Maccarini, M.; Hellweg, T. The Internal Network Dynamics of Poly(NIPAM) Based Copolymer Micro- and Macrogels: A Comparative Neutron Spin-Echo Study. *Z. Phys. Chem.* **2014**, *228*, 1053–1075.

(27) Kyrey, T.; Witte, J.; Feoktystov, A.; Pipich, V.; Wu, B.; Pasini, S.; Radulescu, A.; Witt, M. U.; Kruteva, M.; von Klitzing, R.; Wellert, S.; Holderer, O. Inner Structure and Dynamics of Microgels with Low and Medium Crosslinker Content Prepared *via* Surfactant-Free Precipitation Polymerization and Continuous Monomer Feeding Approach. *Soft Matter* **2019**, *15*, 6536–6546.

(28) Witte, J.; Kyrey, T.; Lutzki, J.; Dahl, A. M.; Houston, J.; Radulescu, A.; Pipich, V.; Stingaciu, L.; Kühnhammer, M.; Witt, M. U.; von Klitzing, R.; Holderer, O.; Wellert, S. A Comparison of the Network Structure and Inner Dynamics of Homogeneously and Heterogeneously Crosslinked PNIPAM Microgels with High Crosslinker Content. *Soft Matter* **2019**, *15*, 1053–1064.

(29) Pospelov, G.; Van Herck, W.; Burle, J.; Carmona Loaiza, J. M.; Durniak, C.; Fisher, J. M.; Ganeva, M.; Yurov, D.; Wuttke, J. BornAgain: Software for Simulating and Fitting Grazing-Incidence Small-Angle Scattering. *J. Appl. Crystallogr.* **2020**, *53*, 262–276.

(30) Pasini, S.; Holderer, O.; Kozielewski, T.; Richter, D.; Monkenbusch, M. J-NSE-Phoenix, a Neutron Spin-Echo Spectrometer with Optimized Superconducting Precession Coils at the MLZ in Garching. *Rev. Sci. Instrum.* **2019**, *90*, 043107.

(31) Zolnierczuk, P. A.; Holderer, O.; Pasini, S.; Kozielewski, T.; Stingaciu, L.; Monkenbusch, M. Efficient Data Extraction from Neutron Time-of-Flight Spin-Echo Raw Data. *J. Appl. Crystallogr.* **2019**, *52*, 1022–1034.

(32) Greaves, G. N.; Greer, A. L.; Lakes, R. S.; Rouxel, T. Poisson's Ratio and Modern Materials. *Nat. Mater.* **2011**, *10*, 823–836.

(33) Rovigatti, L.; Gnan, N.; Ninarello, A.; Zaccarelli, E. Connecting Elasticity and Effective Interactions of Neutral Microgels: The Validity of the Hertzian Model. *Macromolecules* **2019**, *52*, 4895–4906.

(34) Hashmi, S. M.; Dufresne, E. R. Mechanical Properties of Individual Microgel Particles through the Deswelling Transition. *Soft Matter* **2009**, *5*, 3682–3688.

(35) Holderer, O.; Frielinghaus, H.; Wellert, S.; Lipfert, F.; Monkenbusch, M.; von Klitzing, R.; Richter, D. Grazing Incidence Neutron Spin Echo Spectroscopy: Instrumentation Aspects and Scientific Opportunities. *J. Phys. Conf. Ser.* **2014**, *528*, 012025.

(36) Nouhi, S.; Hellsing, M. S.; Kapaklis, V.; Rennie, A. R. Grazing-Incidence Small-Angle Neutron Scattering from Structures below an Interface. *J. Appl. Cryst.* **2017**, *50*, 1066–1074.

(37) Müller-Buschbaum, P. Grazing Incidence Small-Angle Neutron Scattering: Challenges and Possibilities. *Polym. J.* **2013**, *45*, 34–42.

(38) Tokita, M.; Tanaka, T. Friction Coefficient of Polymer Networks of Gels. *J. Chem. Phys.* **1991**, *95*, 4613–4619.

(39) Tanaka, N.; Matsukawa, S.; Kurosu, H.; Ando, I. A Study on Dynamics of Water in Crosslinked Poly (*N*-isopropylacrylamide) Gel by N.M.R. Spectroscopy. *Polymer* **1998**, *39*, 4703–4706.

(40) Gawlitza, K.; Ivanova, O.; Radulescu, A.; Holderer, O.; von Klitzing, R.; Wellert, S. Bulk Phase and Surface Dynamics of PEG Microgel Particles. *Macromolecules* **2015**, *48*, 5807–5815.

(41) Frielinghaus, H.; Gvaramia, M.; Mangiapia, G.; Jaksch, S.; Ganeva, M.; Koutsioubas, A.; Mattauch, S.; Ohl, M.; Monkenbusch, M.; Holderer, O. New Tools for Grazing Incidence Neutron Scattering Experiments Open Perspectives to Study Nano-Scale Tribology Mechanisms. *Nucl. Instrum. Methods Phys. Res., Sect. A* **2017**, *871*, 72–76.

# Graphical TOC Entry